Supporting information to

Night-time oxidation at the air–water interface: co-surfactant effects in two component mixtures.

Federica Sebastiani,[1,2,a] Richard A. Campbell,[2,b] and Christian Pfrang.[1,3,4]

[1] Department of Chemistry, University of Reading, P.O. Box 224, RG6 6AD, Reading, UK
[2] Institut Laue-Langevin, 71 avenue des Martyrs, CS20156, 38042 Grenoble Cedex 9, France
[3] School of Geography, Earth and Environmental Sciences, University of Birmingham, Edgbaston, B15 2TT, Birmingham, UK
[4] Department of Meteorology, University of Reading, P.O. Box 243, RG6 6BB, Reading, UK
[a] current address: Biofilms - Research Center for Biointerfaces, Department of Biomedical Science, Faculty of Health and Society, Malmö University
[b] current address: Division of Pharmacy & Optometry, Faculty of Medicine, Biology & Health, University of Manchester, Oxford Road, Manchester M13 9PT, United Kingdom

Correspondence to: Christian Pfrang (c.pfrang@bham.ac.uk)

1. Materials and Preliminary Characterization

Table 1: List of the organic surfactants used for the experiments including molecular weight (MW) and scattering length (SL). * indicates the custom-deuterated molecules provided by the Oxford Deuteration Facility.

Molecule	Chemical formula	MW / g mol^{-1}	SL / fm
d_{33}MO*	$CD_3(CD_2)_7CD{=}CD(CD_2)_7CO_2CH_3$	329.69	346.80
d_{34}OA	$CD_3(CD_2)_7CD{=}CD(CD_2)_7CO_2D$	316.67	358.05
d_{35}SA	$CD_3(CD_2)_{16}\ CO_2H$	319.69	360.98

The thermodynamic properties of the organic monolayers have been investigated by measuring the pressure isotherm as a function of the surface area on a Langmuir trough.[1] The in-plane structure of the monolayer was monitored with Brewster angle microscopy (BAM) imaging while compressing the film to record the isotherm. We used the Nanofilm EP3 Brewster angle microscope, the instrument is made up by two arms, one where the laser (λ = 532 nm) is mounted and the other where the CCD (Charge-Coupled Device) camera, which records the reflected light, is positioned. Both of the arms are in the plane of the reflection and they form an angle of 53.1° with the normal to the surface. Those two techniques used in combination allowed the characterization of the phase behavior of the binary mixture monolayer, revealing the phase transition regions and the optical properties, such as anisotropy. Both OA and MO in presence of SA show circular domains already at 2-4 mN m^{-1}, the maximum pressure reached by the monolayer of OA-SA (33 mN m^{-1}) is higher than the one composed by MO-SA (17 mN m^{-1}). At the highest pressure, the monolayer OA-SA continues to show circular domains which are closer to each other and points of layer collapse start to arise (bright white spots, Fig. SI1).

The monolayer MO-SA, while it looks similar to OA-SA at low pressure, at high pressure the domains become larger and elongated (Fig. SI3). The further expansion and compression of the same layer shows clear hysteresis, which suggests that those elongated structures are not relaxing back to a mixed monolayer. Hysteresis is found in the MO-SA monolayer too, but to a lower extent. The mixture of MO-OA (Fig. SI2) forms an isotropic monolayer at pressures up to 22 mN m^{-1}, while upon further compression the layer starts to collapse as in the single component monolayer [2].

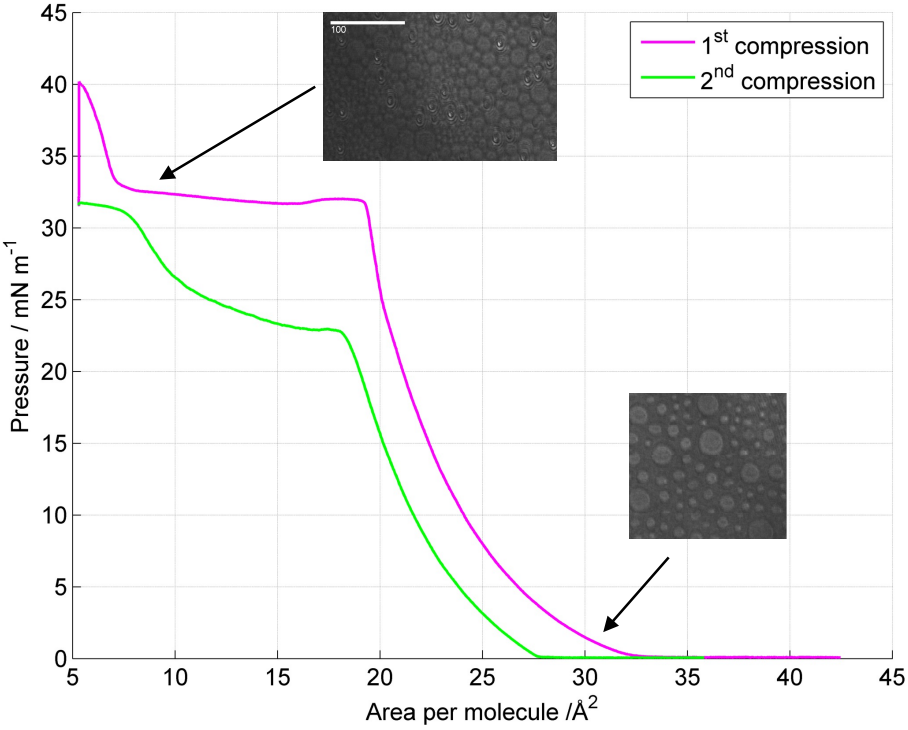

Figure SI1. Surface pressure isotherm of OA-SA at 25°C on a water subphase with the corresponding BAM images of the monolayer recorded at two pressures: 2 mNm^{-1} and 33 mNm^{-1}. At both pressures, the monolayer shows phase separation, with circular domains dispersed in an isotropic background, at the higher pressure the domains become closer and the layer start to collapse in several points. The white bar corresponds to 100 μm.

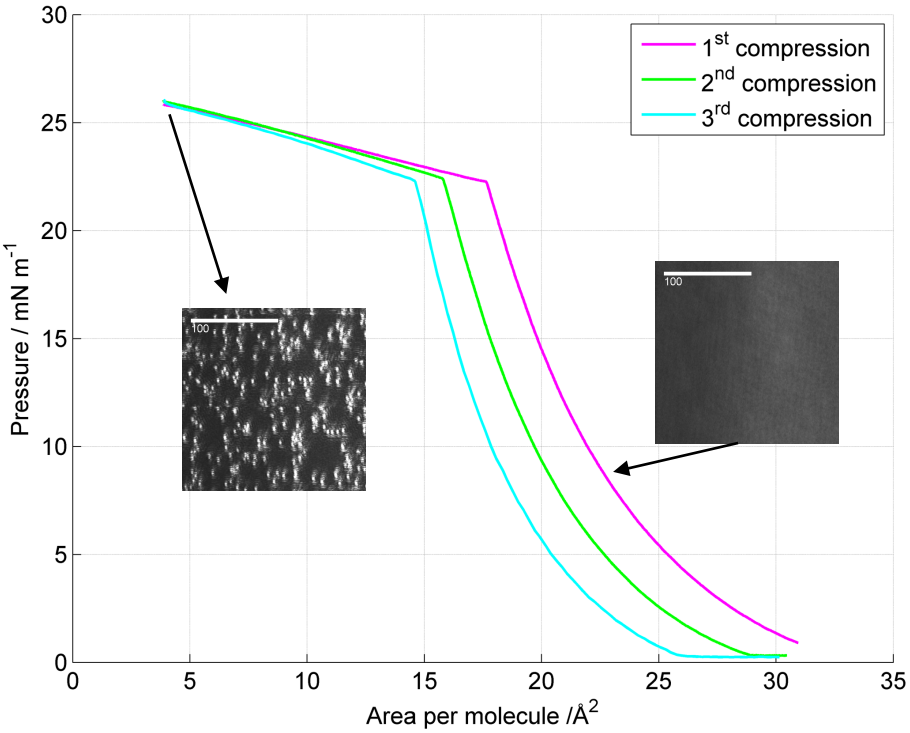

Figure SI2. Surface pressure isotherm of OA-MO at 25°C on a water subphase with the corresponding BAM images of the monolayer recorded at two pressures: 9 mNm^{-1} the layer is isotropic, OA and MO are mixed and 26 mNm^{-1} the layer starts to collapse as for the respective single component monolayer. The white bar corresponds to 100 µm.

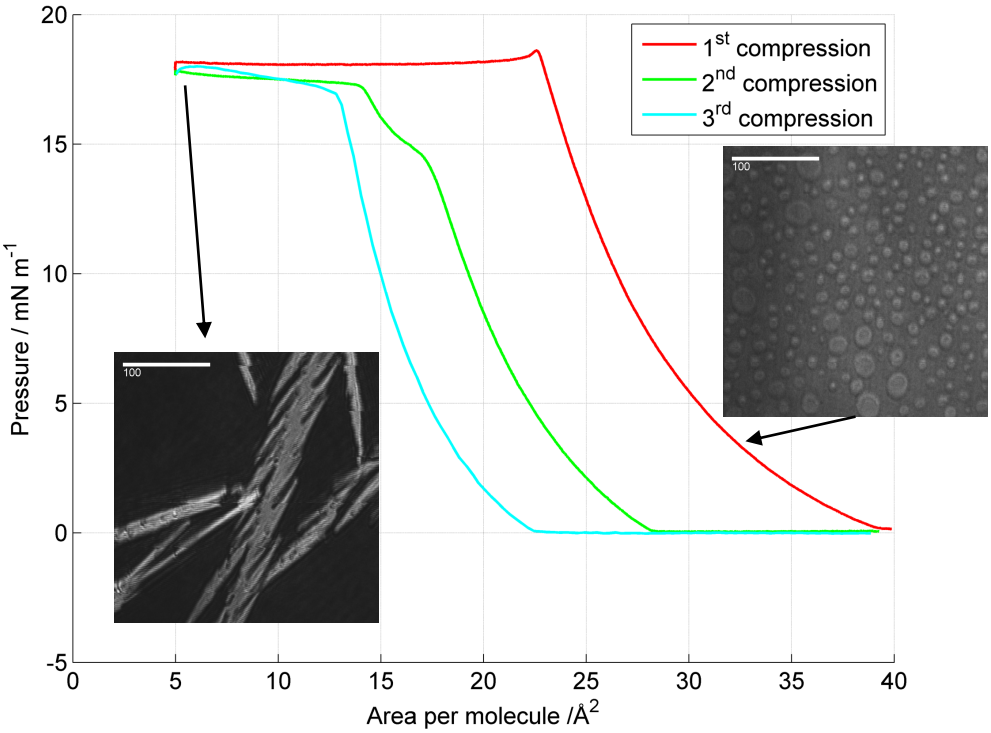

Figure SI3. Surface pressure isotherm of MO-SA at 25°C on a water subphase with the corresponding BAM images of the monolayer recorded at two pressures: 4 mNm^{-1} and 17 mNm^{-1}. At both pressures, the monolayer shows phase separation, at low pressure with circular domains dispersed in an isotropic background, at high pressure the domains become elongated and large. The white bar corresponds to 100 µm.

2. Gas Flow System

Fig. SI4 shows a sketch of the gas flow system. For the production of NO_3, the O_2 flow was kept at 1.2 dm^3 min^{-1} and the flow rate of NO_2 ranged between 0.06 to 0.36 dm^3 cm^{-1}. The mixing bulb has a volume of 5 dm^3, and the inlet part is made of a glass cylinder with 21 small holes on the surface, which enhances mixing of the components. The residence time in the mixing bulb ranges from 2 to 4 minutes, which is long enough to establish equilibrium within the products. The concentration of NO_3 is tuned by changing the NO_2 flow rate and hence its concentration. [NO_2] is always in large excess of [O_3] to ensure that all the ozone is consumed before the gas flow reaches the organic film.

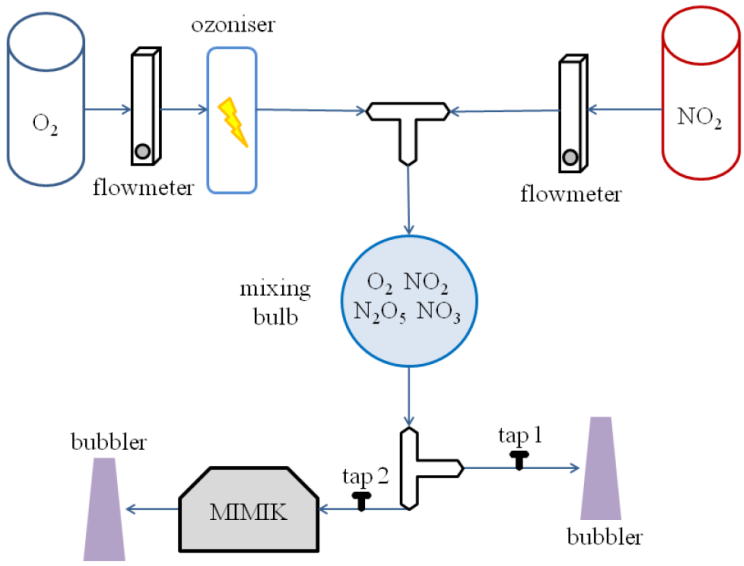

Figure SI4. Schematic of the gas flow system. The arrow represents the direction of the flow. On the top left side the ozone is produced, then it mixes with NO_2 just before the inlet of the mixing bulb. From the mixing bulb the mixture can directly go to an exhaust bubbler or pass through the reaction chamber.

The tubing is made from Chemfluor® (PTFE), with an outer diameter of 1/4 inch and an inner diameter of 1/8 inch; this material has been chosen for its high chemical resistance. A digital flow meter (Model MV-302, MASS–VIEW, Bronkhorst) has been used for the control of the O_2 flow. For the NO_2 a ball flow meter (Cole Parmer) resistant to NO_2 corrosion has been used. All the connectors used were made of Teflon or stainless steel to ensure chemical resistance.

3. Kinetic modelling – theory and results

3.1 Theory

For a complete description of the model, we recommend to check the original work by Sebastiani et al.[2], however we report in the following sections the fundamental concepts of the kinetic modelling.

Accommodation coefficients and desorption lifetimes. The kinetic model used to describe the experimental results depends on several parameters, and some of them are strongly correlated. For example, for a given gas species time evolution, which may be described by certain accommodation coefficients ($\alpha_{s,0,Xi}$ where X_i is NO_3 or NO_2) and certain desorption lifetimes ($\tau_{d,\,Xi}$), a good fit may be obtained as well with a lower $\alpha_{s,0,Xi}$ combined with a higher $\tau_{d,Xi}$. The accommodation coefficient represents the probability of the gas-phase molecule to absorb at the organic layer, hence the lower $\alpha_{s,0,NO3}$ is, the smaller is the probability of the reaction with the organic molecule. The desorption lifetime represents the mean residence time of the

molecule absorbed at the surface, hence the longer this time, the higher is the probability for the gas molecule to react (valid for NO_3). NO_2 does not react with the organic layer [3], but those parameters still compensate, because $\alpha_{s,0,NO2}$ determines the number of molecules absorbed and $\tau_{d,NO2}$ determines the number of molecules leaving the sorption sites. The choice of leaving both of these parameters free to vary in the fitting will lead to a wide range of values for both. The resulting surface excess will match the experimental data. However, the choice of fixing one out of these two parameters makes the optimisation of the model computationally easier and the comparison between different organic molecules possible. In the fitting, we have fixed the $\alpha_{s,0,Xi}$ to one for both gas species.

The desorption lifetime for the reactive species, NO_3, shows a correlation to the reaction rate coefficient, $k_{\mathrm{surf,Y,NO_3}}$, for example if the rate coefficient is kept constant an increase in desorption lifetime will lead to higher loss rate, and vice versa, if $\tau_{\mathrm{d,\,NO_3,eff}}$ is kept constant and $k_{\mathrm{surf,Y,NO_3}}$ increases the loss rate will augment. Our measurement follows the loss rate, the values for $k_{\mathrm{surf,Y,NO_3}}$ and $\tau_{\mathrm{d,\,NO_3,eff}}$ are obtained from the best fit of the model to the data.

Sensitivity study Figure SI5 displays a sensitivity study that demonstrates how the change of desorption lifetimes can affect the model while keeping all the other parameters to the best fit values. A decrease of $\tau_{\mathrm{d,\,NO_3,2}}$ reduces the loss rate, especially for the second half of the decay, while an increase of $\tau_{\mathrm{d,\,NO_3,1}}$ speeds up the decay substantially. A decrease in $\tau_{d,NO2}$ does not affect the model significantly ($\tau_{d,NO2}$ was reduced by four orders of magnitude to see any effect in Fig. SI5), while an increase reduces the loss rate. Figure SI5 demonstrates that the rate coefficients derived through modelling should be quoted together with the desorption lifetimes obtained for the best fit given the substantial impact of changes in the desorption times on the fit to the experimentally observed decays.

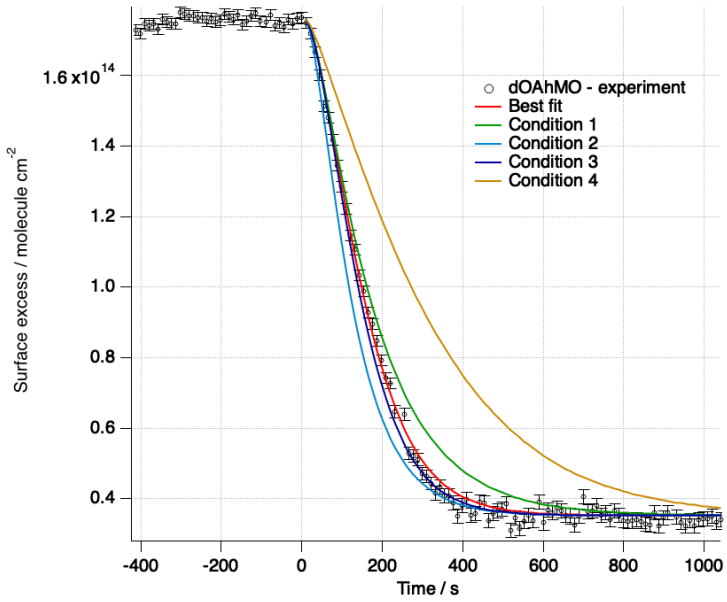

Figure SI5. The experimental data for dOAhMO exposed to $[NO_3]$ = 86 ppt are shown with the best fit in red. The desorption lifetimes for NO_3 and NO_2 have selectively been modified in this sensitivity study to show their effect on the modelled surface excess decay. Condition 1 refers to $\left(\tau_{d,NO_3,1}\right)_{best\ fit} = \tau_{d,NO_3,2}$, and hence $\tau_{d,NO_3,2} = 0.6\left(\tau_{d,NO_3,2}\right)_{best\ fit}$. Condition 2 refers to $\tau_{d,NO_3,1} = \left(\tau_{d,NO_3,2}\right)_{best\ fit}$ and hence $\tau_{d,NO_3,1} = 1.6\left(\tau_{d,NO_3,1}\right)_{best\ fit}$. Condition 3 refers to $\tau_{d,NO2}=10^{-3}\ (\tau_{d,NO2})_{best\ fit}$. Condition 4 refers to $\tau_{d,NO2}=15\ (\tau_{d,NO2})_{best\ fit}$.

Products kinetic and description. Here, we complement the description of the reaction products given in the main text. The volatile products (Z_G) will leave the surface based on their vapour pressures, but with a lack of information on the chemical composition, we decided to use a first-order loss rate coefficient, $k_{loss,G}$, to describe the overall effect, hence the differential equation for Z_G is:

$$\frac{d[Z_G]_{ss}}{dt} = c_G k_{surf,Y,NO_3}\,[Y]_{SS}\,[NO_3]_S - k_{loss,G}[Z_G]_{ss} \qquad (1)$$

where c_G is the branching ratio relative to the volatile products. The bulk–surface transport is not considered for the volatile products because it is assumed to be negligible compared to the volatilisation process. The soluble products (Z_B) will diffuse into the water bulk depending on the diffusion coefficient, $D_{b,B}$, and the transport velocity can be estimated as $k_{bss,B} \approx 4\,D_{b,B}/\pi\delta_B$, where δ_B is the effective molecular diameter of the soluble species. The inverse process is described by a surface–bulk transport velocity $k_{ssb,B} \approx k_{bss,B}/\delta_B$, hence the evolution of the soluble product concentration in surface layer (ss) and bulk (b) is expressed as:

$$\frac{d[Z_B]_{ss}}{dt} = c_B k_{surf,Y,NO_3}\,[Y]_{SS}\,[NO_3]_S + k_{bss,B}[Z_B]_b - k_{ssb,B}[Z_B]_{ss} \qquad (2)$$

$$\frac{d[\mathrm{Z_B}]_b}{dt} = \left(k_{\mathrm{ssb,B}}[\mathrm{Z_B}]_{ss} - k_{\mathrm{bss,B}}[\mathrm{Z_B}]_b\right)\frac{A}{V} \qquad (3)$$

where c_{B} is the branching ratio for the soluble products.

The product branching ratios affect the whole Γ (t), varying c_S the final value of Γ (t) changes, i.e. a higher c_S leads to a higher final value of Γ (t); the model is less sensitive to changes in c_G and c_B, however change in the solubilisation and/or volatilisation kinetic parameters ($D_{\mathrm{b,B}}$ and $k_{\mathrm{loss,G}}$) will affect the decay of Γ (t). These parameters were chosen in order to best describe the experimental data and taking into account literature data.

3.2 Fitting Results

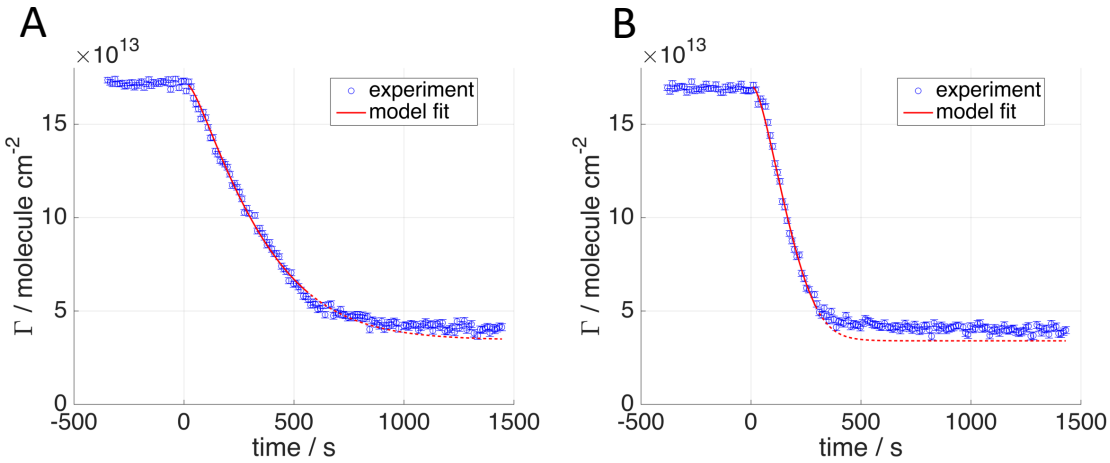

Figure SI6. dOA-hOA: experimental data (blue circles) and model fit (red line): 36 ppt NO3 (A) and 86 ppt NO3 (B).

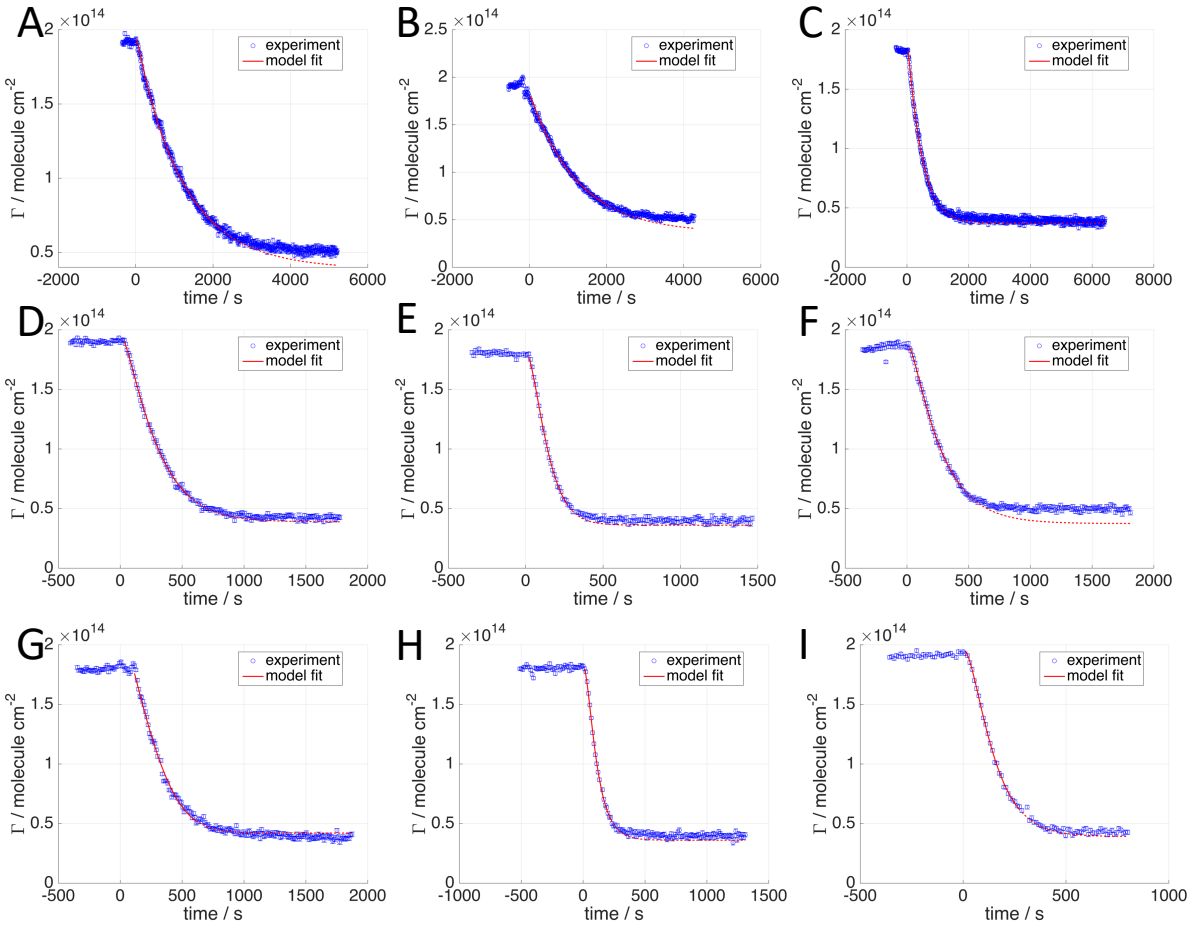

Figure SI7. dOA-hSA: experimental data (blue circles) and model fit (red line): 13 ppt NO3 (A and B), 15 ppt NO3 (C), 32 ppt NO3 (D), 35 ppt NO3 (E), 36 ppt NO3 (F and G), 86 ppt NO3 (H and I).

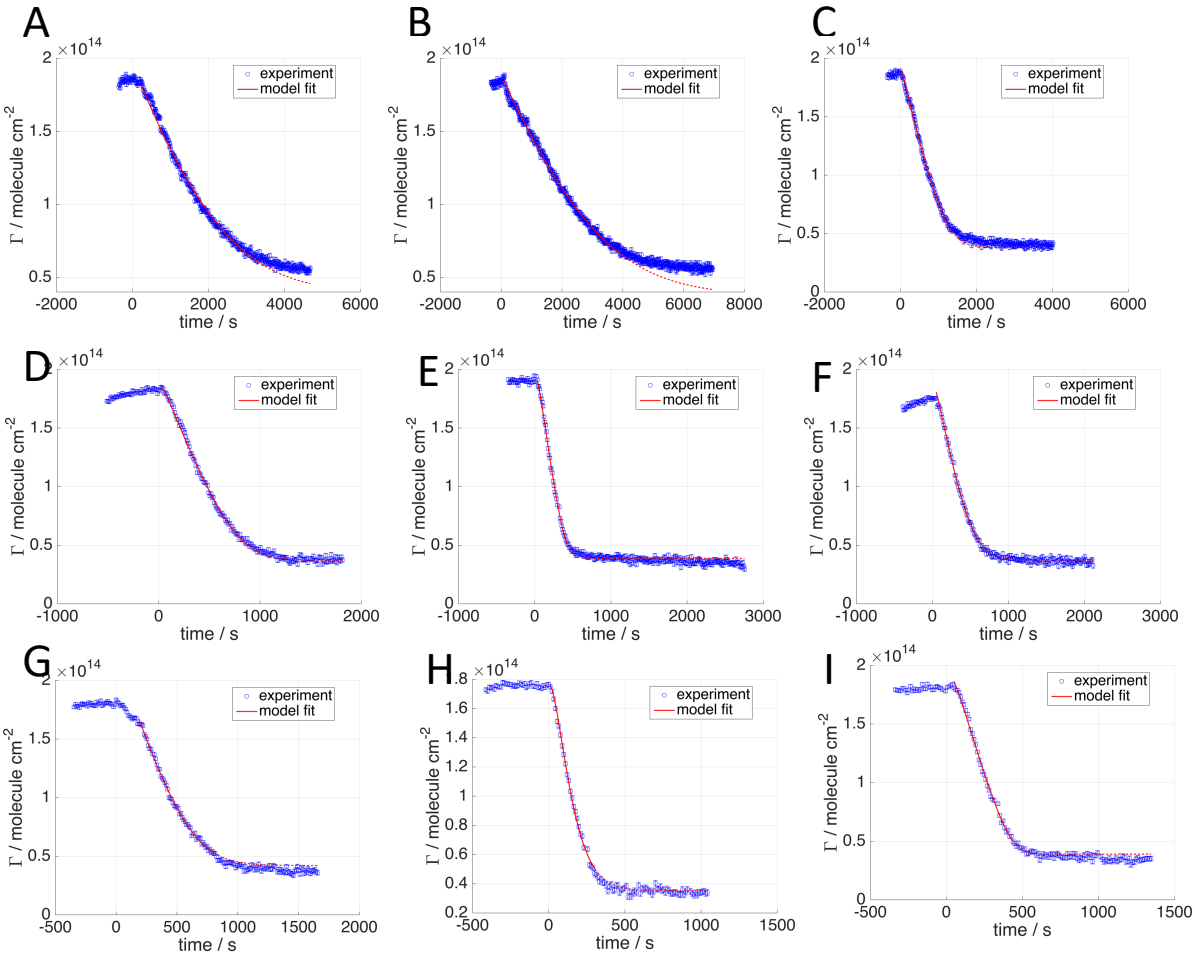

Figure SI8. dOA-hMO: experimental data (blue circles) and model fit (red line): 13 ppt NO3 (A and B), 15 ppt NO3 (C), 32 ppt NO3 (D), 35 ppt NO3 (E), 36 ppt NO3 (F and G), 86 ppt NO3 (H and I).

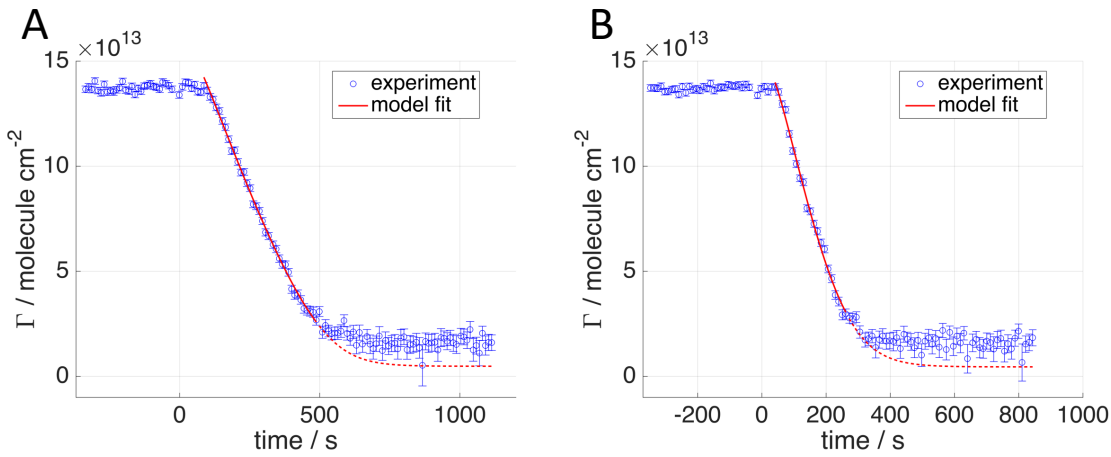

Figure SI9. dMO-hMO: experimental data (blue circles) and model fit (red line): 36 ppt NO3 (A) and 86 ppt NO3 (B).

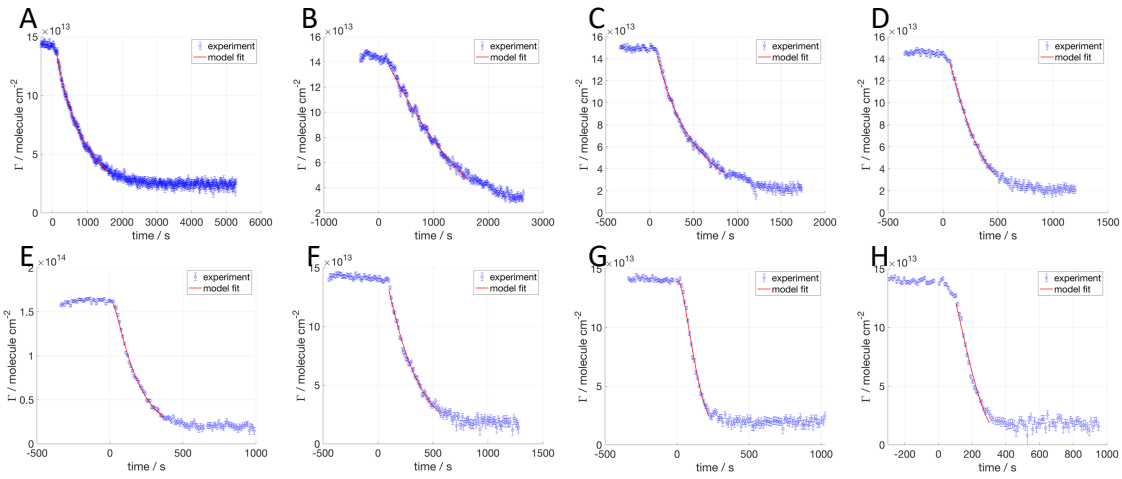

Figure SI10. dMO-hSA: experimental data and model fit: 13 ppt NO3 (A and B), 15 ppt NO3 (C), 32 ppt NO3 (D), 36 ppt NO3 (E and F), 86 ppt NO3 (G and H).

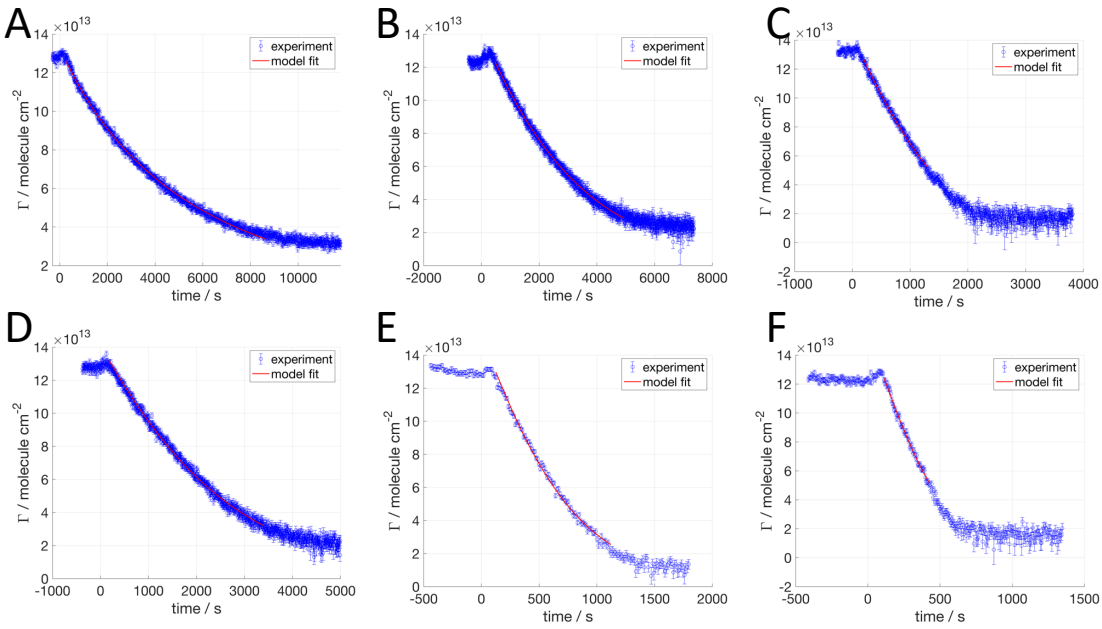

Figure SI11. dMO-hOA: experimental data and model fit: 23 ppt NO3 (A), 32 ppt NO3 (B), 35 ppt NO3 (C), 36 ppt NO3 (D), 86 ppt NO3 (E) and 100 ppt NO3 (F).

References

1 G. Barnes and I. Gentle, *Interfacial science: an introduction*, Oxford University Press, 2nd edn., 2010.

2 F. Sebastiani, R. A. Campbell, K. Rastogi and C. Pfrang, Night-time oxidation of surfactants at the air–water interface: effects of chain length, head group and saturation., *Atmos. Chem. Phys.*, 2018, **18**, 3249–3268.

3 M. D. King, A. R. Rennie, C. Pfrang, A. V Hughes and K. C. Thompson, Interaction of nitrogen dioxide (NO2) with a monolayer of oleic acid at the air–water interface – A simple proxy for atmospheric aerosol, *Atmos. Environ.*, 2010, **44**, 1822–1825.